G-Mode Magnetic Force Microscopy: Separating magnetic and electrostatic interactions using big data analytics

Liam Collins,[1,2] Alex Belianinov,[1,2] Roger Proksch, [3] Tingting Zuo,[4,5]Yong Zhang,[4] Peter K. Liaw,[5] Sergei V. Kalinin, [1,2] Stephen Jesse[1,2]

[1]Center for Nanophase Materials Sciences, Oak Ridge National Laboratory, Oak Ridge, Tennessee 37831, USA

[2]Institute for Functional Imaging of Materials, Oak Ridge National Laboratory, Oak Ridge, Tennessee 37831, USA

[3] Asylum Research, an Oxford Instruments Company, Santa Barbara, CA, USA

[4]State Key Laboratory for Advanced Metals and Materials, University of Science and Technology Beijing, Beijing 100083, China

[5]Deptarment of Materials Science and Engineering, University of Tennessee, Knoxville, Tennessee 37996-2200, USA

Abstract

Here we develop a full information capture approach for Magnetic Force Microscopy (MFM), referred to as generalized mode (G-Mode) MFM. G-Mode MFM acquires and stores the full data stream from the photodetector at sampling rates approaching the intrinsic photodiode limit. The data can be subsequently compressed, denoised, and analyzed, without information loss. Here,

G-Mode MFM is implemented and compared to traditional heterodyne based MFM on model systems including domain structures in ferromagnetic Yttrium Iron Garnet (YIG) and electronically and magnetically inhomogeneous high entropy alloy, CoFeMnNiSn. We investigate the use of information theory to mine the G-Mode MFM data and demonstrate its usefulness for extracting information which may be hidden in traditional MFM modes, including signatures of nonlinearities and mode coupling phenomena. Finally we demonstrate detection and separation of magnetic and electrostatic tip-sample interactions from a single G-Mode image, by analyzing the entire frequency response of the cantilever. G-Mode MFM is immediately implementable on any AFM platform and as such is expected to be a useful technique for probing spatiotemporal cantilever dynamics and mapping material properties as well as their mutual interactions.

Keywords

Atomic Force Microscopy (AFM), Magnetic Force Microscopy (MFM), Multivariate Analysis

Magnetic force microscopy (MFM)[1] is a non-contact variant of Atomic Force Microscopy, (AFM)[2] which allows visualization of the nanoscale magnetic field above a sample surface. MFM is a valuable tool with a rich history[3] in characterization of a variety of materials and devices including nanoparticles,[4] ultra-thin films,[5] memory storage devices,[6] ferromagnetic materials,[7] superconducting materials,[8] and even biological systems.[9] In MFM, a ferromagnetic AFM tip, attached to a flexible cantilever, is brought into proximity with the surface of a sample. Stray magnetic fields from the sample generate forces and force gradients on the magnetic tip that affects the response of the cantilever. As the tip is scanned across the surface, both the magnetic field and the topography can be mapped and correlated.

Direct interpretation of the magnetic force maps in MFM, is not straight forward, and can be obscured by incomplete information of the micromagnetic structure of the tip, dynamic changes of tip- and sample magnetization state during imaging (including both losses and Barhausen jumps), non-linear cantilever dynamics, and non-magnetic interactions.[10-14] In the classical implementation of MFM, based on resonant frequency detection, all these interactions are mixed, yielding a single image. Hence, separation of different magnetic mechanisms as well as differentiating magnetic signal from other long range interactions remains an essential problem to MFM.

Here we develop an MFM approach utilizing full information capture of the tip-surface interaction, and contrast our findings to the classical heterodyne detection approach. We utilize recently developed general mode, (G-Mode)[15] AFM, which has previously been demonstrated for AFM tapping mode,[15] piezoresponse force microscopy[16] and Kelvin probe force microscopy.[17] G-Mode samples the entire photodetector response in time domain at a sampling rate of ~4MHz, as the tip scans the surface at constant velocity. The resulting data can be

reshaped into a 3-dimensional array by segmenting the data stream into x-position bins containing the cantilever deflection signal as a function of time within that bin. Note that division of the fast-scan-axis information into pixels can be performed after acquisition, enabling multiresolution imaging.[15,17] The resulting data file is typically on the order or 4GB for the equivalent of a 256 x 256 pixel image taking approximately 18 minutes to capture (e.g. comparable to standard MFM). In contrast, standard MFM images are small (~1 MB), 2D matrices of the time averaged amplitude and phase (or resonant frequency) signals. In the case of G-Mode, dynamic processes (including non-periodic, rare events and transients), are encoded in the tip trajectory, captured in the data stream, and available for further analysis. Here, we demonstrate that G-Mode can be used to emulate conventional MFM, as well as discover signatures of non-linear interactions that are lost during heterodyne detection using information theory analysis techniques.[18-23] Finally, we demonstrate a route to simultaneous electrostatic and magnetic property mapping in a single G-Mode image dataset obtained at regular scanning rates.

Measurements were performed on an Asylum Research Cypher microscope, with as-received Co/Cr-coated (Asylum Research, ASYMFMHM) AFM probes, with a nominal mechanical resonance frequency and spring constant of 70 kHz and 2.0 N/m, respectively. The tips were magnetized prior to use by bringing them into close proximity with a strong magnet. In this work we used photothermal excitation[24,25] (i.e. BlueDrive^{TM}) to achieve a clean mechanical excitation of the cantilever. As has been previously shown on a similar sample, a flat, clean cantilever drive improves the separation of conservative and dissipative magnetic interactions.[26] Standard MFM measurements were performed in dual pass mode at 50 nm lift height, using phase sensitive detection. For G-Mode imaging we used Matlab and LabView software for control and post processing. National Instruments PXIe-1073 coupled with the NI PXIe-6214 DAQ architecture

was used to generate an AC cantilever excitation waveform and to capture the photodetector signal. As a model system for magnetic domain imaging, we have chosen a ferromagnetic Yttrium iron garnet (YIG, $Y_3Fe_5O_{12}$) sample.[27,28,29] For a system having both compositional and magnetic inhomogeneity we investigate a high entropy alloy[17,30,31] with a nominal composition of CoFeMnNiSn.

In conventional MFM, the cantilever is driven at a fixed frequency while either the frequency or phase of the cantilever is recorded as a 2D map. These observables can be interpreted in terms of both the local force gradient and tip-sample dissipation.[1] The frequency/phase is measured by heterodyne detection, which effectively time averages the response of the cantilever at each pixel.

An example of G-Mode MFM results on YIG are shown in Figure 1. Here, we utilize principal component analysis (PCA), as a fast and computationally inexpensive, first step in separating data into orthonormal components in descending order of statistical significance based on variance.[32,33] Each principal component comprises an eigenvalue loading map as well as an eigenvector. The pair can be used to interpret the type of behavior, (eigenvector) and its spatial variation (loading map). For comparison the AFM topography and standard MFM imaging of the same region are provided in the supplementary information, see Fig. S1 (a,b,c), along with the results from digital based heterodyne analysis on the G-Mode MFM data (see Fig. S1(d,e,f)).

The results of the PCA analysis of the G-Mode data are shown in Figure 1, where Figure 1(a-d) depicts the first 4 loading maps and Fig. (e-h) represents their corresponding eigenvectors respectively. The first 3 principal components represent 98.36% of the statistically significant variance in the data, with subsequent components largely dominated by noise without observable

spatial variation. The loading maps of the first and third principal components depict "flower-like" magnetic domain patterns, characteristic for this material and matching the contrast to the phase maps detected using heterodyne detection (Fig. S1).[34] The corresponding eigenvectors for the first and third components are dominated by a single peak (in the frequency domain) located at the drive frequency (75.16 kHz), which indicates that the loading maps correspond to a magnetic interaction alone. The second principal component shows weaker spatial contrast relating to the magnetic domains. The inset of Figure 1(g) depicts a segment of the second and third eigenvectors in the time domain demonstrating a clear phase shift with respect to each other and the corresponding loading maps suggest this shift is related to changes in the force gradient as a result of the tip-sample magnetic interactions. Finally, the fourth PC loading map which has no discernible spatial contrast, and is likely related to noise in the measurement or microscope instrumentation. The corresponding eigenvector, Fig. 1(h) corroborates this finding as there is no response at the driving frequency, and the eigenvector frequency spectrum is dominated by 1/f noise and thermal noise around the resonance frequency.

These results demonstrate that G-Mode combined with information theory analysis can be used to emulate conventional MFM, and that the vast majority of the information pertaining to tip-sample interactions is contained at a single frequency (drive frequency). It also demonstrates, however, that PCA effectively reduces the dimensionality, allowing visualization of the high dimensional data sets without fitting to a physical model. Furthermore, the approach can be harnessed to effectively de-noise the signal by rejecting uncorrelated information without a priori knowledge using a purely statistical approach. For example, the data could be reconstructed from the first three principal components alone (eigenvectors and loadings), and the other noise dominated principal components could be rejected.

We further proceed to analyze the spatial information present in the G-Mode PCA loading maps in an attempt to discern other possible tip-sample interactions which may be encoded in the complex dataset but having weak informational weight with respect to the total response. In order to do this we calculate the radially averaged correlation function C(r) of the loading maps where by definition C(0)=1. In the presence of discernible features the correlation function will have a long-range tail, whereas images populated by noise have rapidly decaying tails (Cr), where, in the limit of random noise C(r>0) = 0. We also calculate the scree plot for the principal components which represents the informational weight as a function of principal component number. Fig. 2(a) illustrates the radial auto correlation function results for PCA produced images as a function of eigenvector C(r, n). Note that the first three components contain discernible spatial features, whereas subsequent components contain either very short-range features (for example, topographic edges and so on) or are noise dominated. Surprisingly, some of the senior components contain long-range correlations as well, as can be confirmed by visual inspection of the loadings maps. In particular the loading maps of the 7^{th} and 10^{th} principal components can be identified to be moderately correlated from inspection of Figure 2(a), and are shown to have spatial variation corresponding to magnetic domains, Fig 2(c) and (e). To investigate this further, the loading maps are plotted with a contour overlay of the YIG magnetic domains determined from Figure 1(a) (images without contour map are provided in Fig S2). Noteworthy, this highly correlated spatial variation corresponds to very small informational weight as determined from the skree plot where the 7^{th} and 10^{th} principal component correspond to 0.039% and 0.032% percentage of the total variation. Furthermore, the corresponding eigenvectors show antisymmetric type of behavior of the excitation peak which can indicate a shift in the resonance frequency. Interestingly these principal components seem to be confined to

locations where the tip crosses over magnetic domain walls as well as showing alternating variability for similar domains. This might suggest that these weak components correspond to phenomena related to abrupt changes in the cantilever dynamics which could induce a change in magnetization state in either tip or sample. From Figure 2(a) it is clear that discernible features are expected in principal components 13-15 as the correlation function for these principal components show a long long-range tail. Figure 2(g) and (e) depict the loading map and eigenvector respectively, which show spatial information unrelated to the samples magnetic properties, and an eigenvector which is dominated by a response peak located at 25 kHz far from the excitation frequency of the cantilever (75 kHz). This type of behavior is also representative of the 14 and 15 components and is believed to be related to microscope or instrumentation effects. Components 13-15 collectively equate to 0.04% of the overall informational weight.

Noteworthy, heterodyne detection methods are extremely sensitive to the response at the drive frequency and its harmonics; however, such approaches do not allow for recovering information outside the detection frequency (e.g. intermodulation products[35,36] etc.). An obvious advantage to collecting and storing an entire spectrogram is the ability to unravel the cantilever response at each frequency, without repeating the measurement. In Figure 3 we leverage this capability to simultaneously map magnetic properties and electrostatic properties of the high entropy (HEA) alloy CoFeMnNiSn. Often HEAs contain domain structures having differing electronic and magnetic properties,[30,37-39] hence, the ability to probe these properties simultaneously, on the nanoscale, would be greatly beneficial for correlation of material microstructure with functionality. First we map the topography, work function and magnetic variation across the sample using standard Kelvin probe force microscopy (KPFM)[40] and MFM respectively, see Figure 3(a, c, d). By performing these measurements sequentially and

comparing them we can conclude the presence of at least two domains which have very different electronic and magnetic properties since this alloy is expected to contain an $L2_1$-structured matrix rich in Ni, Mn, and Sn and body centered cubic (BCC)-structured second phase which is rich in Fe and Co.

For G-Mode, we demonstrate simultaneous magnetic and electrostatic mapping by photo-thermally driving the cantilever at the mechanical resonance ω_0, and modulating the electrical signal far from resonance (3 kHz). We perform the measurement over the same sample area shown in Figure 3(a). As seen in Figure 3(b), the response is rich in harmonics and mixing products as a result of the non-linear interaction between the tip and sample. This nonlinearity generates sidebands around the resonance frequency ω_0 at $\omega_0 \pm \omega_{el}$ and $\omega_0 \pm 2\omega_{el}$. This has some similarities to frequency modulated KPFM,[41] which relies on sideband generation governed by the electrostatic force gradient as opposed to the electrostatic force. When this data is analyzed using a digital LIA, we observed clear contrast in both amplitude and phase for all harmonics. In this way, G-Mode allows capturing a large number (~8000) frequency information channels simultaneously, without sacrificing data quality. We utilize the dual harmonic detection[42,43] to determine the contact potential difference (CPD),[17,42,43] opting to use the direct electrostatic force components (A_ω and $A_{2\omega}$) to avoid indirect crosstalk of the side bands with shifts in the mechanical resonance frequency, with the trade of poorer signal to noise compared to on resonance KPFM. Denoising of the G-Mode KPFM data can be performed using PCA and/or noise thresholding as has previously be described.[44]

Selected PCA analysis of the data, shown in Figure 3, is provided in supplementary information (Fig S3 and S4) for comparison. In this case however, the complex tip-sample interactions result in the statistically significant data being spread across more principal

components, as is expected for the multiple excitations and responses, and the electrostatic response in principal components 11-13th collectively amounts to 0.38 % of the total signal. G-Mode MFM provides deeper insight into the surface processes by allowing simultaneous mapping of CPD, (see Figure 3(g)) and capacitance gradient (see Figure 3(f)) channels; as well as increased flexibility in data exploration across frequency, time, space, and noise domains.[17]

To summarize, we have demonstrated an approach for mapping magnetic domains based on MFM combined with full photo-detector data capture and subsequent multivariate analytics, or software based LIA. G-Mode MFM produces temporally resolved maps of magnetic domains in a broad frequency window. This temporal component may prove useful in probing transient or dynamic magnetic phenomena in the future, to be utilized in mapping dynamic processes such as motion of domain walls at timescales on the order of the tip oscillation. To deal with the size and dimensionality of the G-Mode dataset, we have explored multivariate statistical analysis to visualize pertinent behavior and to reduce dimensionality and size of the data. A similar process, albeit utilizing a different algorithm, can be used to fit statistical results to physical parameters. PCA is shown to be an initial, fast method used to explore cantilever dynamics and extract material properties. Finally, we demonstrated simultaneous mapping, and de-mixing of magnetic and electrostatic interactions by capturing the entire cantilever response spectra allowing for simultaneous mapping of work function variation and magnetic interactions. In the future this temporally resolved approach once implemented on low noise platforms may prove useful for detection and imaging of electron spin relaxation in quantum computing or spintronic devices,[45] as has been demonstrated with magnetic resonance force microscopy.[46]

Acknowledgements

This research(for L. C., A. B., S. V. K., S. J.) was conducted at the Center for Nanophase Materials Sciences, which is a DOE Office of Science User Facility. PKL would like to acknowledge the DOE, Office of Fossil Energy, National Energy Technology Laboratory (DE-FE-0008855, DE-FE-0024054, and DE-FE-0011194). PKL appreciates the support of the U.S. Army Research Office project (W911NF-13-1-0438) and the support for the National Science Foundation (CMMI-1100080).

References

[1] Y Martin and H Kumar Wickramasinghe, Applied Physics Letters **50** (20), 1455 (1987).

[2] G. Binnig, C. F. Quate, and C. Gerber, Phys. Rev. Lett. **56** (9), 930 (1986).

[3] U Hartmann, Annual review of materials science **29** (1), 53 (1999).

[4] Victor F Puntes, Pau Gorostiza, Deborah M Aruguete, Neus G Bastus, and A Paul Alivisatos, Nature materials **3** (4), 263 (2004).

[5] M Dreyer, M Kleiber, A Wadas, and R Wiesendanger, Physical Review B **59** (6), 4273 (1999).

[6] Stuart SP Parkin, Masamitsu Hayashi, and Luc Thomas, Science **320** (5873), 190 (2008).

[7] Feng Bi, Mengchen Huang, Sangwoo Ryu, Hyungwoo Lee, Chung-Wung Bark, Chang-Beom Eom, Patrick Irvin, and Jeremy Levy, Nat. Commun. **5** (2014).

[8] A Wadas, O Fritz, HJ Hug, and H-J Güntherodt, Zeitschrift für Physik B Condensed Matter **88** (3), 317 (1992).

[9] Roger B Proksch, TE Schäffer, BM Moskowitz, ED Dahlberg, Dennis A Bazylinski, and Richard B Frankel, Applied Physics Letters **66** (19), 2582 (1995).

[10] Hans J Hug, B Stiefel, PJA Van Schendel, A Moser, R Hofer, S Martin, H-J Güntherodt, Steffen Porthun, Leon Abelmann, and JC Lodder, Journal of Applied Physics **83** (11), 5609 (1998).

[11] J Lohau, S Kirsch, A Carl, G Dumpich, and EF Wassermann, Journal of applied physics **86** (6), 3410 (1999).

[12] JM Garcıa, André Thiaville, J Miltat, KJ Kirk, JN Chapman, and F Alouges, Applied Physics Letters **79** (5), 656 (2001).

[13] A Asenjo, Miriam Jaafar, D Navas, and M Vázquez, Journal of applied physics **100** (2), 023909 (2006).

[14] Thomas Häberle, Felix Haering, Holger Pfeifer, Luyang Han, Balati Kuerbanjiang, Ulf Wiedwald, Ulrich Herr, and Berndt Koslowski, New Journal of Physics **14** (4), 043044 (2012).

[15] A. Belianinov, S. V. Kalinin, and S. Jesse, Nature Communications **6** (2015).

[16] Suhas Somnath, Alexei Belianinov, Sergei V Kalinin, and Stephen Jesse, Applied Physics Letters **107** (26), 263102 (2015).

[17] Liam Collins, Alex Belianinov, Suhas Somnath, Brian J Rodriguez, Nina Balke, Sergei V Kalinin, and Stephen Jesse, Nanotechnology **27** (10), 105706 (2016).

[18] Liam Collins, Stephen Jesse, Jason I Kilpatrick, Alexander Tselev, Oleksandr Varenyk, M Baris Okatan, Stefan AL Weber, Amit Kumar, Nina Balke, Sergei V Kalinin, and BJ Rodriguez, Nature communications **5** (2014).

[19] Alex Belianinov, Rama Vasudevan, Evgheni Strelcov, Chad Steed, Sang Mo Yang, Alexander Tselev, Stephen Jesse, Michael Biegalski, Galen Shipman, and Christopher Symons, Advanced Structural and Chemical Imaging **1** (1), 1 (2015).

[20] Rama K Vasudevan, Alex Belianinov, Anthony G Gianfrancesco, Arthur P Baddorf, Alexander Tselev, Sergei V Kalinin, and Stephen Jesse, Applied Physics Letters **106** (9), 091601 (2015).

[21] Alex Belianinov, Panchapakesan Ganesh, Wenzhi Lin, Brian C Sales, Athena S Sefat, Stephen Jesse, Minghu Pan, and Sergei V Kalinin, APL Materials **2** (12), 120701 (2014).

[22] Evgheni Strelcov, Alexei Belianinov, Ying-Hui Hsieh, Ying-Hao Chu, and Sergei V Kalinin, Nano letters **15** (10), 6650 (2015).
[23] E. Strelcov, A. Belianinov, Y. H. Hsieh, S. Jesse, A. P. Baddorf, Y. H. Chu, and S. V. Kalinin, ACS Nano **8** (6), 6449 (2014).
[24] Glenn C Ratcliff, Dorothy A Erie, and Richard Superfine, Applied physics letters **72** (15), 1911 (1998).
[25] A Labuda, K Kobayashi, Daniel Kiracofe, K Suzuki, PH Grütter, and H Yamada, AIP Advances **1** (2), 022136 (2011).
[26] Roger Proksch and Sergei V Kalinin, Nanotechnology **21** (45), 455705 (2010).
[27] S Geller and MA Gilleo, Journal of Physics and Chemistry of Solids **3** (1), 30 (1957).
[28] M Abe and M Gomi, Journal of magnetism and magnetic materials **84** (3), 222 (1990).
[29] AC Rastogi, VN Moorthy, and Sandip Dhara, Applied Physics Letters **78** (2001).
[30] Yong Zhang, Ting Ting Zuo, Zhi Tang, Michael C Gao, Karin A Dahmen, Peter K Liaw, and Zhao Ping Lu, Progress in Materials Science **61**, 1 (2014).
[31] Ming-Hung Tsai and Jien-Wei Yeh, Materials Research Letters **2** (3), 107 (2014).
[32] Ian Jolliffe, *Principal component analysis*. (Wiley Online Library, 2002).
[33] Hervé Abdi and Lynne J Williams, Wiley Interdisciplinary Reviews: Computational Statistics **2** (4), 433 (2010).
[34] A Wadas, John Moreland, Paul Rice, and RR Katti, Applied physics letters **64** (9), 1156 (1994).
[35] Daniel Platz, Erik A Tholén, Devrim Pesen, and David B Haviland, Applied Physics Letters **92** (15), 153106 (2008).
[36] Riccardo Borgani, Daniel Forchheimer, Jonas Bergqvist, Per-Anders Thorén, Olle Inganäs, and David B Haviland, Applied Physics Letters **105** (14), 143113 (2014).
[37] PF Yu, LJ Zhang, H Cheng, H Zhang, MZ Ma, YC Li, G Li, PK Liaw, and RP Liu, Intermetallics **70**, 82 (2016).
[38] Tingting Zuo, Xiao Yang, Peter K Liaw, and Yong Zhang, Intermetallics **67**, 171 (2015).
[39] Yong Zhang, TingTing Zuo, YongQiang Cheng, and Peter K Liaw, Scientific reports **3** (2013).
[40] M Nonnenmacher, MP o'Boyle, and HK Wickramasinghe, Applied physics letters **58** (25), 2921 (1991).
[41] Th Glatzel, S Sadewasser, and M Ch Lux-Steiner, Applied Surface Science **210** (1), 84 (2003).
[42] Liam Collins, Jason I Kilpatrick, Ivan V Vlassiouk, Alexander Tselev, Stefan AL Weber, Stephen Jesse, Sergei V Kalinin, and Brian J Rodriguez, Applied physics letters **104** (13), 133103 (2014).
[43] Liam Collins, JI Kilpatrick, Stefan AL Weber, Alexander Tselev, Ivan V Vlassiouk, Ilia N Ivanov, Stephen Jesse, SV Kalinin, and BJ Rodriguez, Nanotechnology **24** (47), 475702 (2013).
[44] L. Collins, A. Belianinov, S. Somnath, BJ Rodriguez, N. Balke, S. V. Kalinin, and S. Jesse, Nanotechnology **Accepted** (2016).
[45] BC Stipe, HJ Mamin, CS Yannoni, TD Stowe, TW Kenny, and D Rugar, Phys. Rev. Lett. **87** (27), 277602 (2001).
[46] JOHN A Sidles, JOSEPH L Garbini, KJ Bruland, D Rugar, O Züger, S Hoen, and CS Yannoni, Reviews of Modern Physics **67** (1), 249 (1995).

Figure Captions

Figure. 1. (a-d) First four principal components and (g-h) and there corresponding eigenvectors from PCA analysis of a G-Mode MFM scan on a YIG sample.

Figure 2. (a) 2D radially averaged correlation function results for the different eigenvector loadings from the data shown in Figure 3 of the manuscript distributed over. (b) PCA Skree plot on a log-log scale. (c,d) Seventh, (e,f) 10^{th} and (g,h) 13^{th} principal component (c,e,g) loading map and (d,f,h) eigenvector. Eigenvectors are shown in the time domain representation in insets of (d,f,h). The contour map on was generated from the first principle component and overlayed on the (c) and (e) for visualization purposes.

Figure 3. (a) AFM topography of a CoFeMnNiSn HEA. (b) Single pixel FFT response showing multiple harmonics and sideband generation. Variation in (C) contact potential difference and (d) magnetic domains determined using conventional KPFM and MFM consecutively. LIA analysis of G-Mode data showing (e) A_{ω} and (f) $A_{2\omega}$ which were used to determine the open loop (g) CPD. (h) Shows the simultaneously recorded magnetic domain response from LIA analysis of the mechanical excitation at ω_0.

Figures

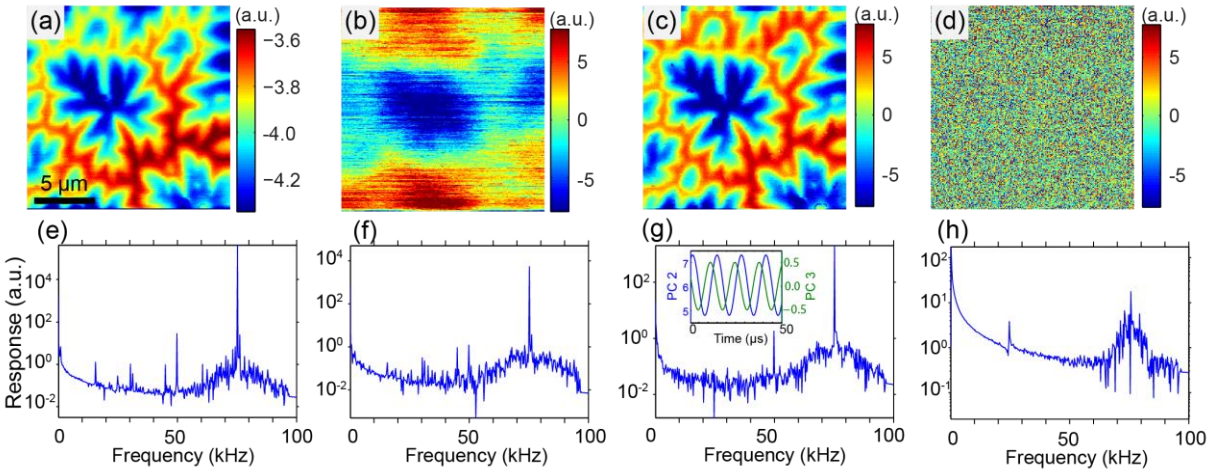

Figure 1. Collins et al.

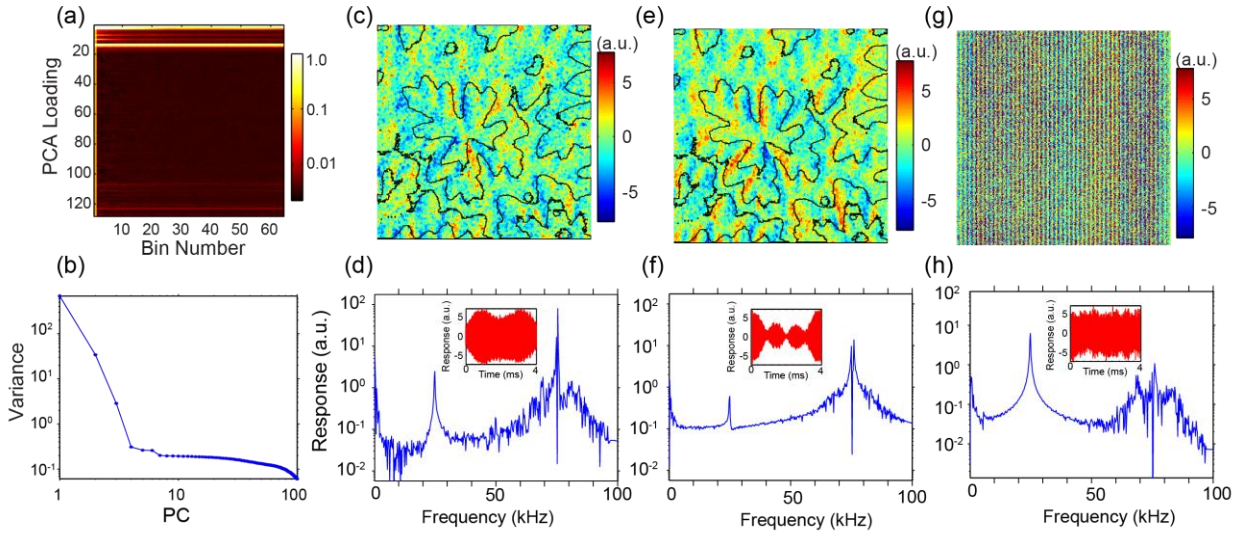

Figure 2. Collins et al.

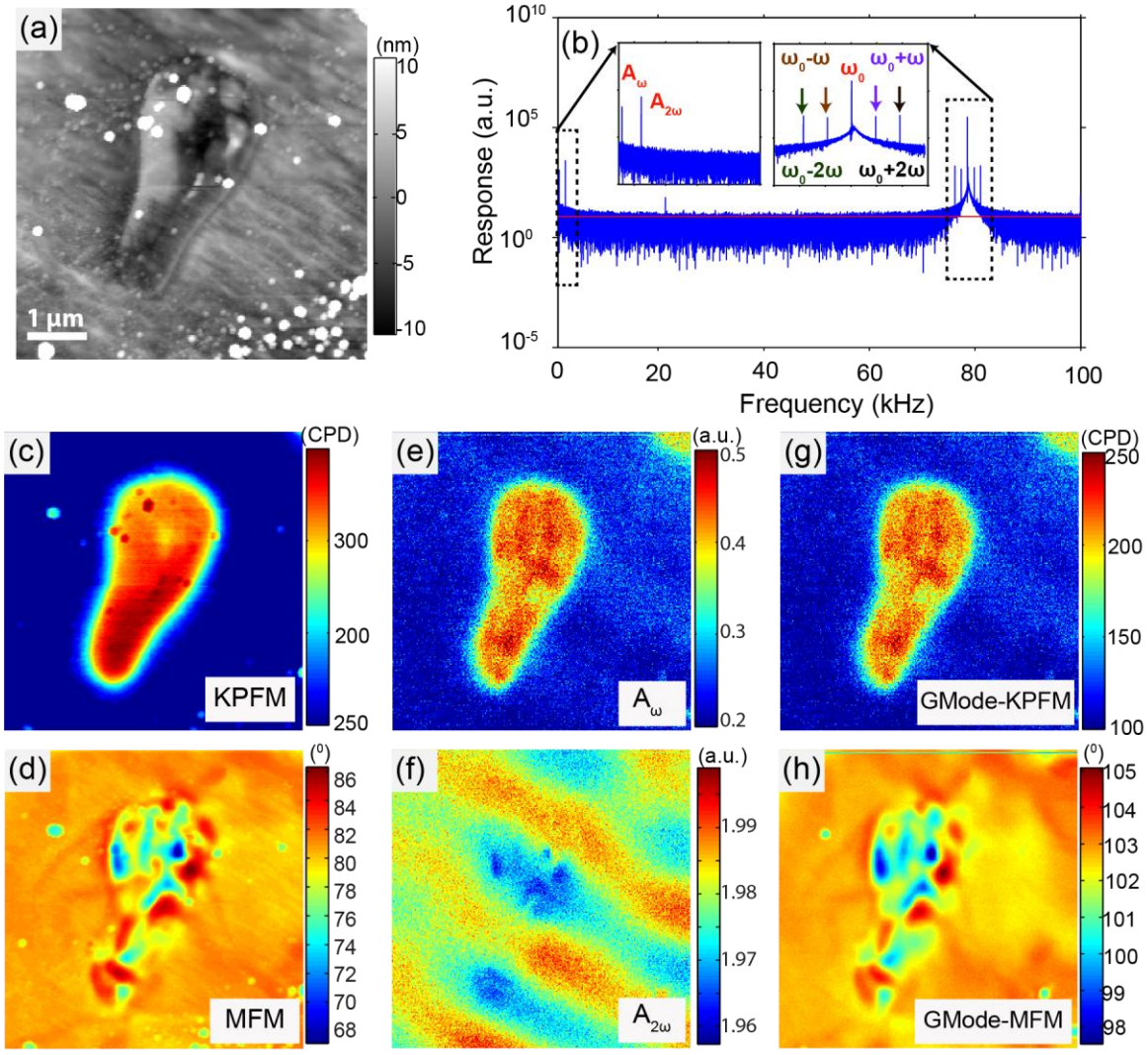

Figure 3. Collins et al.

[1]